PROCEEDINGS OF SPIE

Dual-comb spectroscopic polarimetry for dynamic characterization of polarization property

Koresawa, Hidenori, Gouryeb, Marc, Shibuya, Kyuki, Mizuno, Takahiko, Hase, Eiji, et al.

Dual-comb spectroscopic polarimetry for dynamic characterization of polarization property

Hidenori Koresawa,[a] Marc Gouryeb,[a,b] Kyuki Shibuya,[a,c,d] Takahiko Mizuno,[c,d,e] Eiji Hase,[d,e] Yu Tokizane,[e] Ryo Oe,[a] Takeo Minamikawa,[c,d,e] and Takeshi Yasui*[c,d,e]

[a]Graduate School of Advanced Technology and Science, Tokushima University, 2-1 Minami-Josanjima, Tokushima, Tokushima 770-8506, Japan
[b]College of Sciences and Technology, University of Bordeaux, 351 cours de la Libération, Talence Cedex 33405, France
[c]Graduate School of Technology, Industrial and Social Sciences, Tokushima University, 2-1 Minami-Josanjima, Tokushima, Tokushima 770-8506, Japan
[d]JST, ERATO, MINOSHIMA Intelligent Optical Synthesizer Project, 2-1 Minami-Josanjima, Tokushima, Tokushima 770-8506, Japan
[e]Institute of Post-LED Photonics (pLED), Tokushima University, 2-1 Minami-Josanjima, Tokushima, Tokushima 770-8506, Japan

ABSTRACT

Spectroscopic polarimetry (SP) is a powerful tool for characterization of thin film, polarization optics, semiconductor, and others. However, mechanical polarization modulation of broadband light hampers its application for dynamic monitoring of a sample. In this article, we demonstrate the dynamic SP with features of polarization-modulation-free polarimetry and spectrometer-free spectroscopy benefiting from dual-comb spectroscopy (DCS) using a pair of optical frequency combs (OFCs). DCS enables the direct determination of polarization without the need for polarization modulation by using mode-resolved OFC spectra of amplitude and phase for two orthogonally linear-polarized lights while securing rapid, high-precision, broadband spectroscopy without the need for spectrometer. Effectiveness of the proposed system is highlighted by visualizing the hysteresis property of dynamic response in a liquid-crystal-on- silicon spatial light modulator at a sampling rate of 105 Hz.

Keywords: Spectroscopic polarimetry, Optical frequency comb, Dual-comb spectroscopy

1. INTRODUCTION

Spectroscopic polarimetry (SP) [1–11] is based on simultaneous measurement of polarization and spectrum before and after a broadband light is incident onto a sample. Since change of polarization and spectrum reflects optical property of the sample sensitively, SP is a powerful tool for material characterization in field of fundamental science, industry, and bioscience. For example, spectroscopic ellipsometry [1–9], which is a representative SP with an oblique-incidence reflection configuration, has been applied for evaluation of refractive index and thickness of thin film [1–3], material property such as optical bandgap [4,5] and biosensing of antibody-antigen reaction [6–8].

SP measures broad spectra of a phase difference Δ and an amplitude ratio ψ between two orthogonally linear-polarized lights (x-polarization component and y-polarization component in transmission configuration or p-polarization component and s-polarization component in reflection configuration) when the broadband light with known polarization is incident onto the sample. To obtain these spectra, a spectrum of optical intensity is measured while modulating the polarization of the incident or the output light, and the resulting spectrum is used for determining the spectra of Δ and ψ. Depending on methods of polarization modulation, SP can be classified into three types: rotating-analyzer SP [9], rotating-compensator SP [10], and phase modulation SP [11]. The rotating-analyzer SP and the rotating-compensator SP acquire the spectra of Δ and ψ by a combination of a multi-channel spectrometer with a mechanically rotating polarization optics. Although these SPs have own advantages such as easy implementation and moderate precision, such mechanical polarization modulation limits the mechanical stability and the data acquisition time (typically, several tens

of milliseconds) of the SP system. On the other hand, the phase modulation SP benefits from non-mechanical, rapid polarization modulation with a photoelastic modulator (PEM), and hence can reduce the data acquisition time (typically, several tens of microseconds). However, since phase modulation with PEM shows a large dependent on the wavelength and the temperature, the precise compensation of phase modulation is required for SP. Furthermore, the fast modulation speed with PEM (tens of kilohertz) is not so good compatible with the use of a multi-channel spectrometer equipped with a camera (frame rate = $10 \sim 1000$ fps). These features make it difficult to apply PEM for broadband SP. In other words, PEM is often used in the monochromatic polarimetry rather than SP. Recently, optical frequency comb (OFC) [12–14] has attracted attention as a light source for broadband spectroscopy because it can be used as a precise ruler of optical frequency or wavelength by control of a frequency spacing f_{rep} and carrier-envelope-offset frequency f_{ceo} in comb-tooth-like ultra-discrete multimode spectrum. Full potential of OFC can be used by acquiring mode-resolved OFC spectra of amplitude and phase with dual-comb spectroscopy (DCS) [15–18]. DCS acquires an interferogram between a pair of OFCs with slightly different repetition frequency without the need for mechanical scanning, and then obtains the mode-resolved OFC spectra of amplitude and phase by Fourier transform of the acquired interferogram. Due to its precise, accurate, and rapid acquisition of the broadband spectrum, DCS has been used for spectroscopic applications; examples include gas spectroscopy [19,20], gas thermometry [21], solid spectroscopy [22], hyper-spectral imaging [23], and coherent Raman imaging [24]. Furthermore, DCS has been combined with several modulation techniques for spectroscopic polarimetry [25,26].

More recently, DCS was applied for spectroscopic ellipsometry without the need for polarization modulation, namely dual-comb spectroscopic ellipsometry or DCSE [27]. In DCSE, ultrahigh- resolution spectra of Δ and ψ is directly obtained from mode-resolved OFC spectra of amplitude and phase for the p-polarization component and s-polarization component of the output light. Such polarization-modulation-free approach benefits from the immunity to mechanical vibrational noise, thermal instability, and polarization-wavelength dependency, which were often problems in existing mechanical-modulation-based or non-mechanical-modulation-based SP. Effectiveness of DCSE was successfully demonstrated in the determination of thickness in SiO_2 film on Si substrate. On the other hand, there is a considerable need for dynamic monitoring of SiO_2 film process in semiconductor production and antibody-antigen reaction in biosensing. DCSE is one potential candidate for such dynamic monitoring because it has a potential to boost the data acquisition rate up to kilohertz due to its modulation free capability and rapid spectroscopy.

In this article, for proof of concept in dynamic DCSE, we constructed dual-comb SP with a normal-incidence reflection configuration, we here call it DCSP, and apply it for investigation of dynamic property of a liquid-crystal-on-silicon spatial light modulator.

2. EXPERIMENTAL SETUP

Figure 1 shows an experimental setup of DCSP. A pair of mode-locked erbium-doped fiber OFCs (Neoark Co., Japan, OCLS-HSC-D100-TKSM, center wavelength = 1562 nm, spectral bandwidth = 50 nm; OFC1, f_{ceo1} = 10.5 MHz, f_{rep1} = 100 MHz ; OFC2, f_{ceo2} = 10.5 MHz, f_{rep2} = 99.99895 MHz; $\Delta f_{rep} = f_{rep2} - f_{rep1}$ = 1050 Hz) were used for light sources in DCSP. While f_{ceo1}, f_{rep1}, and f_{ceo2} are phase-locked to a rubidium frequency standard (Rb-FS, Stanford Research Systems, Inc., FS725, frequency = 10 MHz, accuracy = 5×10^{-11}, instability = 2×10^{-11} at 1 s), the OFC2 was tightly and coherently locked to the OFC1 with a constant Δf_{rep} using a narrow-linewidth continuous-wave (CW) laser (CWL, Redfern Integrated Optics, Inc., Santa Clara, California, USA, PLANEX, center wavelength = 1550 nm, FWHM < 2.0 kHz) for an intermediate laser via control of f_{rep2} [20,22,23]. This enables coherent averaging of the interferogram between the OFC1 and OFC2.
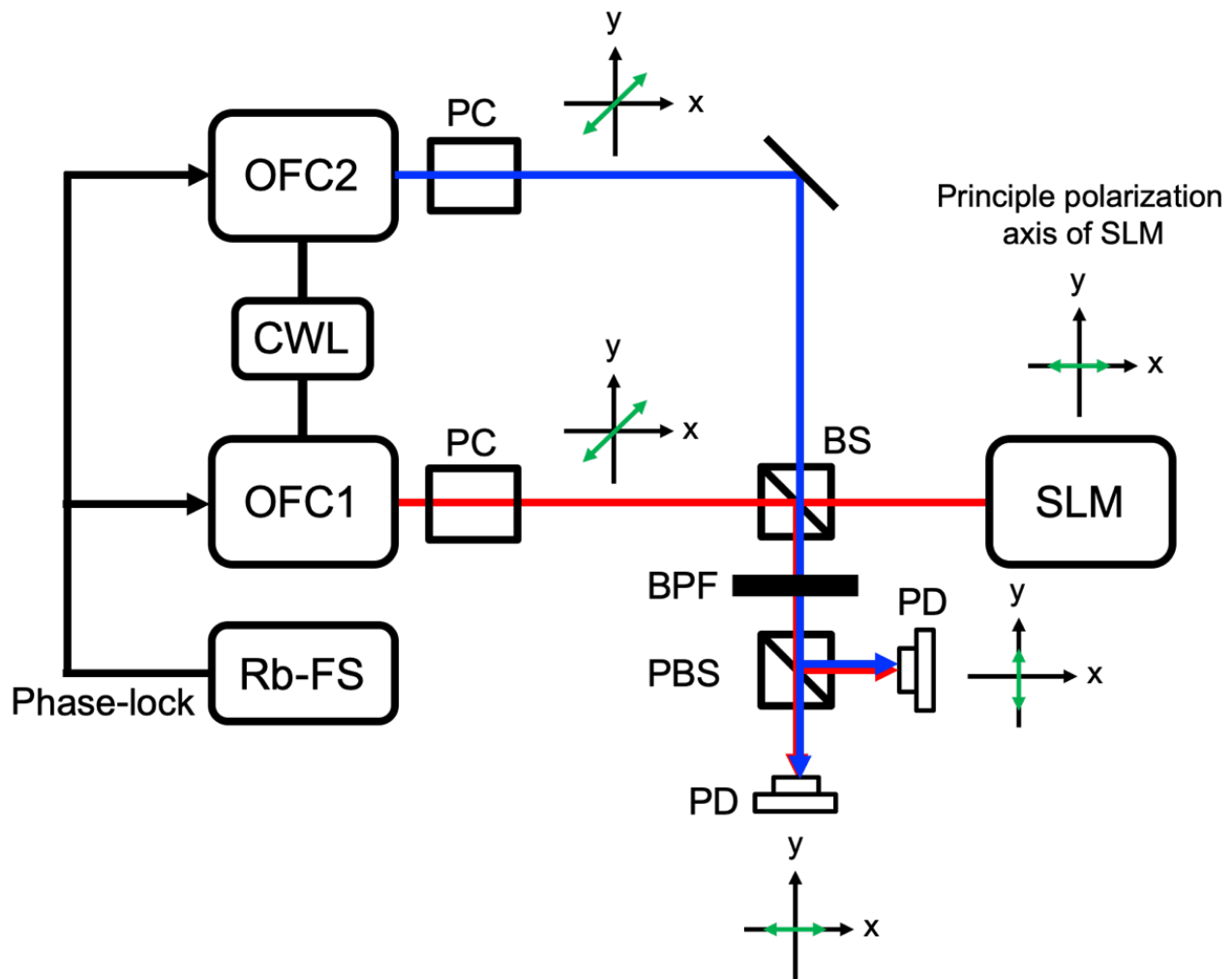
Figure 1. Experimental setup. OFC1 and OFC2, optical frequency combs; CWL, narrow-linewidth CW laser; Rb-FS, rubidium frequency standard; PC, polarization controller; BS, non-polarizing beamsplitter cube; SLM, reflective spatial light modulator; BPF, 1560 ±12 nm band-pass filter; PBS, polarization beam splitter; PDs, photodetectors.

We here define x- and y-polarization components to be horizontally- and vertically-polarized components, respectively. Linear polarization of two OFCs was directed at an angle of +45° to x-polarization component using a polarization controller (PC, extinction ratio = 100,000). After passing through a non-polarizing beamsplitter cube (BS, Thorlabs Inc., Newton, NJ, USA, BS018, split ratio = 50:50), the OFC1 light was incident to a sample perpendicular to its surface. We here used a reflective spatial light modulator based on liquid crystal on silicon (LCOS) technology (SLM, Santec, Komaki, Aichi, Japan, SLM-100, phase stability < 0.002π rad, phase resolution = 10 bit) for a dynamic sample. Principal polarization axis of SLM was set to be parallel to x-polarization component, which tilts by -45° from the polarization angle of OFC1 beam. We confirmed the normal incidence of the OFC1 to the SLM surface by checking the spatial overlapping between the incident light and the reflected light. For more precise analysis, the parameter fitting of the model function for SLM will be useful. After being reflected by the sample, the OFC1 light was spatially overlapped with the OFC2 light with +45° linear polarization by BS. This results in generation of the interferogram between the OFC1 and OFC2. An optical band-pass filter (BPF, Thorlabs Inc., Newton, NJ, USA, FB1560-12, pass band = 1560 ± 12 nm) was used to suppress the aliasing effect in the acquisition of the interferogram. The x-polarization component and y-polarization component of the generated interferogram was separated by a polarization beam splitter (PBS, Thorlabs Inc., Newton, NJ, USA, PBS104, extinction ratio > 1,000), and then was detected by a pair of photodetectors (PDs, Thorlabs Inc., Newton, NJ, USA, PDA10CF-EC, wavelength = 800-1700 nm, RF bandwidth < 150 MHz). Temporal waveform of the detected electric signal was acquired by a digitizer (National Instruments Corp., Austin, Texas, USA, NI PCI-5122,

sampling rate = f_{rep2} = 99,998,950 samples/s, number of sampling points = 95237, resolution = 14 bit). The acquisition rate of interferogram were equal to Δf_{rep}. We acquired consecutive interferograms and integrated them as necessary to obtain appropriate signa-to-noise ratio. Fourier transform of acquired temporal waveforms gives the mode-resolved OFC spectra of amplitude and phase in the *x*-polarization component and *y*-polarization component of the interferogram. The resulting spectra were used for calculation of the Δ and ψ spectra of the sample. We beforehand measured an instrumental function of DCSP by using a gold flat mirror as a standard material and calibrated the experimental data of a sample by comparing between them.

3. RESULT

3.1 Static characterization of SLM

The SLM used here generates arbitrary 2D phase patterns on a LCOS pixel-by-pixel basis by changing a control parameter for SLM, namely SLM grayscale value. We first investigated the change of Δ and ψ in SLM by DCSP when the SLM grayscale value in the solid image is changed from 0 to 960 step by step at interval of 120. We acquired 1000 temporal waveforms of interferogram (total acquisition time = 952 ms), integrated them, and performed Fourier transform of it. Red pots of Figs. 2(a) and 2(b) show 3D plots of Δ and ψ with respect to optical frequency (= 191.5 ∼ 192.5 THz, sampling interval = f_{rep1}) and SLM grayscale value (= 0, 120, 240, 360, 480, 600, 720, 840, and 960). For comparison, specification values of SLM for Δ and ψ are indicated as mesh surface. Little dependence of Δ and ψ on optical frequency was confirmed due to flat optical-frequency response of SLM and/or the limited spectral bandwidth of OFC1. On the other hand, the Δ plot shows a linear dependence on the SLM grayscale value while the ψ plot maintains the constant value with respect to the SLM grayscale value ($\approx$ 0.8 rad). Since SLM changes only the optical phase of the *x*-polarization component to the fixed optical phase of the *y*-polarization component in the reflected light at this configuration, the behavior of Δ well reflects the polarization modulation by SLM: +45° linearly polarized light for $\Delta = 0$ rad, right-handed circularly polarized light for $\Delta = \pi/2$ rad, +135° linearly polarized light for $\Delta = \pi$ rad, left-handed circularly polarized light for $\Delta = 3\pi/2$ rad, and +225° linearly polarized light for $\Delta = 2\pi$ rad, respectively. The +45° linearly polarized light for $\Delta = 0$ rad is equivalent to the +225° linearly polarized light for $\Delta = 2\pi$ rad although there is a large difference of SLM grayscale value between them. In this way, the SLM could cover the optical phase change over 2π.

To evaluate Δ and ψ in SLM more precisely, we extracted the data of Δ and ψ at 192.000 THz from Figs. 2(a) and 2(b) as shown by red plots in Figs. 2(c) and 2(d). For comparison, we indicate specification values of SLM as blue lines in Figs. 2(c) and 2(d). The measure values of Δ and ψ were good agreement with the specification value of them. When the measurement accuracy of Δ and ψ (Δ_{RMSE} and ψ_{RMSE}) is defined as a root mean square error (RMSE) between the measured value and the specification value in Δ and ψ, ΔRMSE and ψ_{RMSE} were 1.6×10^{-1} rad and 1.4×10^{-2} rad, respectively. The reason why Δ_{RMSE} is an order of magnitude more than ψ_{RMSE} might be due to polarization dependence of complexed reflectance or transmittance in detection optics such as BS and PBS.

(a)   (b)

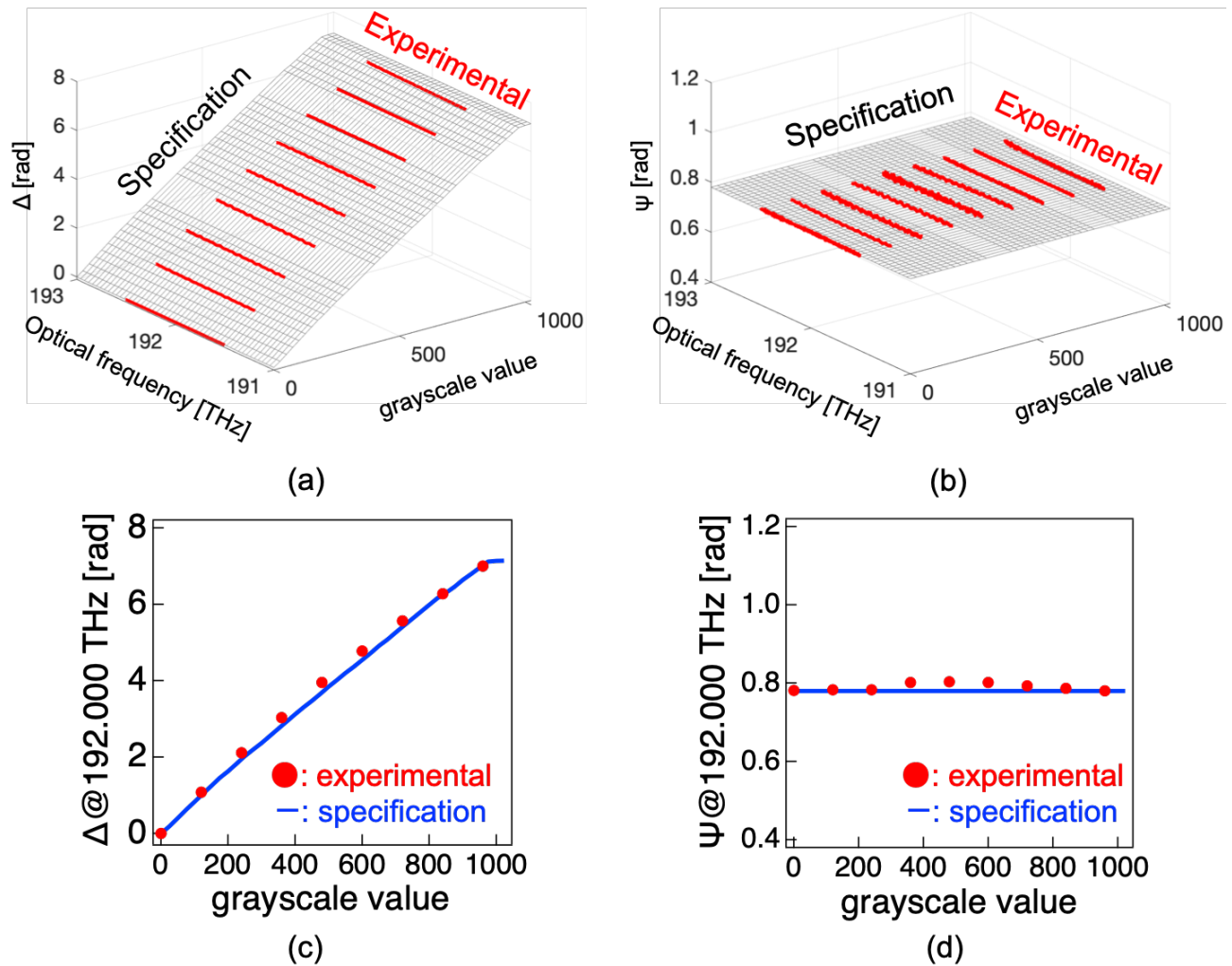(c)   (d)

Fig. 2. Static characterization of Δ and ψ in SLM. 3D plots of (a) Δ and (b) ψ with respect to optical frequency and SLM grayscale value. (c) Δ and (d) ψ at 192.000 THz with respect to SLM grayscale value.

We next investigated the temporal stability of Δ and ψ in SLM when its SLM grayscale value was set to be a fixed value of 500. We here define the standard deviation of Δ and ψ (Δ_{STD} and ψ_{STD}) as their temporal stability. Red plots in Figs. 3(a) and 3(b) show Δ_{STD} and ψ_{STD} at 192.000 THz with respect to the accumulation time, respectively. For comparison, we also measured Δ_{STD} and ψ_{STD} at 192.000 THz as indicated by blue plots in Figs. 3(a) and 3(b) when a gold flat mirror was set as a sample. Δ_{STD} and ψ_{STD} at 192.000 THz was decreased in them when the accumulation time was increased. Also, Δ_{STD} and ψ_{STD} in SLM was higher than those in the mirror, implying a little instability of Δ and ψ in SLM. Δ_{STD} at an accumulation time of 1 s for SLM was reasonably coincides with the specification value of phase stability in SLM (< 0.002π rad).
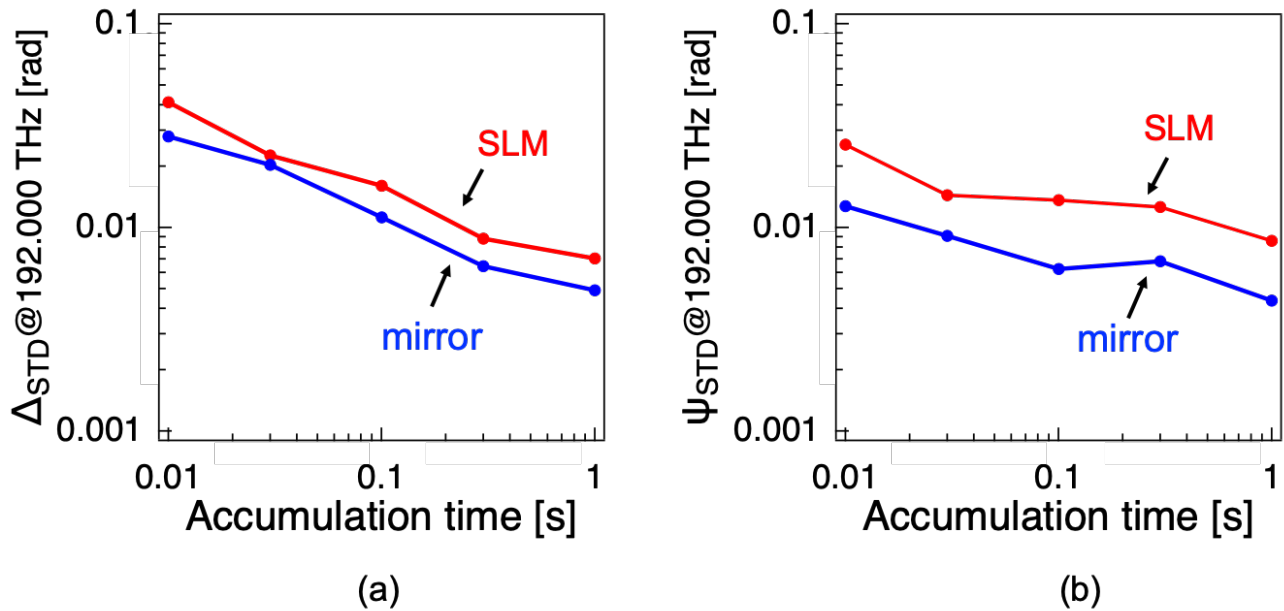
Figure 3 Temporal stability of (a) Δ and (b) ψ with respect to accumulation time in SLM.

3.2 Dynamic characterization of SLM

We next investigated characteristics of temporal response in SLM. To this end, we measured the transient change of Δ and ψ in SLM by DCSP when the SLM grayscale level in the solid image was changed as a step function from 0 to 190 which corresponds to change of polarization from a + 45° linearly polarized light to a right-handed circularly polarized light. We acquired 10 temporal waveforms of interferogram (total acquisition time = 9.52 ms), integrated them, and performed Fourier transform of it. Δ and ψ were obtained at a sampling interval of 9.52 ms within a time window size of 3.5 s by repeating the procedure above. Figure 4(a) and 4(b) shows 3D plots of Δ and ψ with respect to optical frequency and elapsed time. Δ shows similar behavior reflecting a step-function-like change at all optical frequencies while ψ maintained the same level before and after the change of polarization.
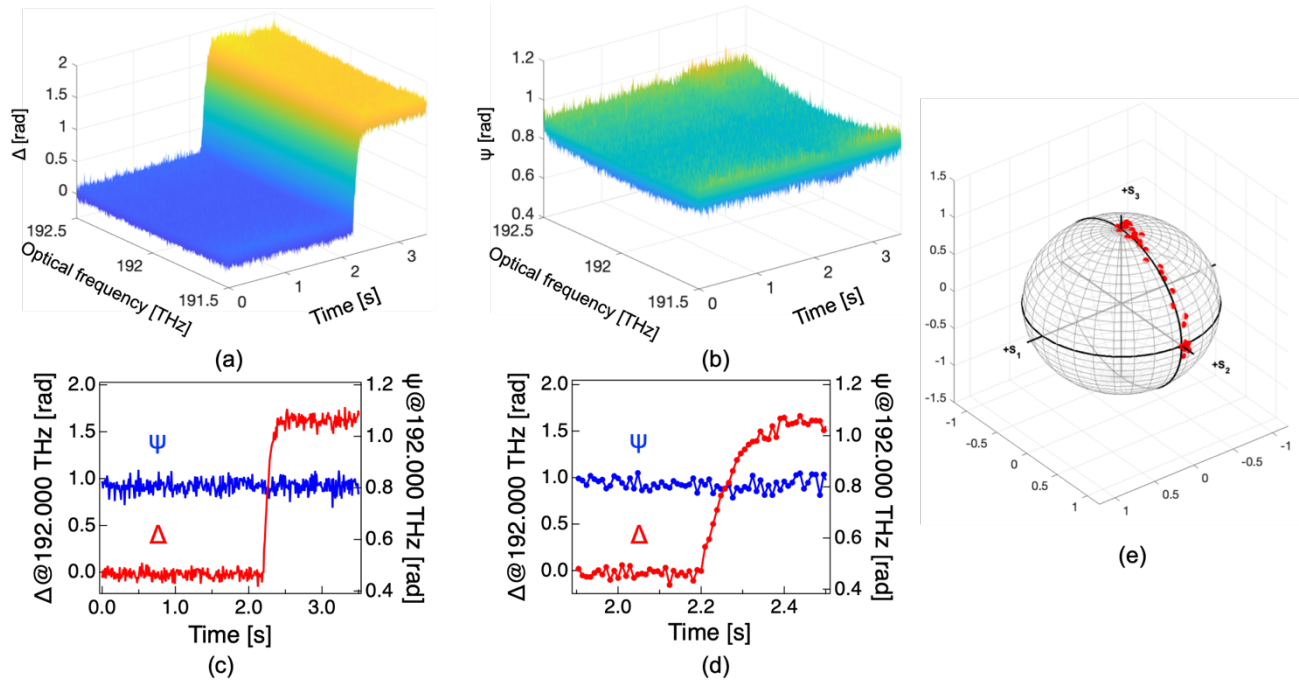
Fig. 4. Dynamics characterization of Δ and ψ in SLM. 3D plots of (a) Δ and (b) ψ with respect to optical frequency and elapsed time. Temporal response of Δ and ψ at 192.000 THz within the time range of (c) 0 to 3.5 s and (d) 1.89 s to 2.51 s. (e) Trajectory of polarization change on the Poincare sphere.

To evaluate the temporal dynamics of Δ and ψ in SLM more precisely, we extracted the data of Δ and ψ at 192.000 THz from Figs. 4(a) and 4(b) as shown by red and blue plots in Fig. 4(c). Figure 4(d) shows temporally magnified plots of Δ and ψ in the vicinity of a rising edge of Δ in Fig. 4(c). Somewhat blunt response of Δ to the step-function-like input was confirmed by a sufficient number of sampling points in DCSP. From Δ and ψ in Fig. 4(d), we visualized the dynamic change of polarization before and after the rising edge as plots on the Poincare sphere in Fig. 4(e). Here, Poincare parameters (S_0, S_1, S_2, and S_3) are given as follows

$$S_0 = E_x^{\,2} + E_y^{\,2}, \tag{1}$$

$$S_1 = E_x^{\,2} - E_y^{\,2}, \tag{2}$$

$$S_2 = 2E_x E_y \cos\Delta, \tag{3}$$

$$S_3 = 2E_x E_y \sin\Delta, \tag{4}$$

where Ex and Ey are x-polarization and y-polarization components of optical electric field. When S_0 is normalized, Eqs. (1) to (4) are transformed as follows

$$S_0 = 1, \tag{5}$$

$$S_1 = \frac{E_x^{\,2} - E_y^{\,2}}{E_x^{\,2} + E_y^{\,2}} = \frac{1 - \tan^2\psi}{1 + \tan^2\psi}, \tag{6}$$

$$S_2 = \frac{2E_x E_y \cos\Delta}{E_x^{\,2} + E_y^{\,2}} = \frac{2\tan\psi \cos\Delta}{1 + \tan^2\psi}, \tag{7}$$

Downloaded From: https://www.spiedigitallibrary.org/conference-proceedings-of-spie on 25 Mar 2021
Terms of Use: https://www.spiedigitallibrary.org/terms-of-use

$$S_3 = \frac{2E_x E_y \sin\Delta}{E_x{}^2 + E_y{}^2} = \frac{2\tan\psi \sin\Delta}{1+\tan^2\psi}. \tag{8}$$

Plots on the Poincare sphere clearly indicate a straight trajectory from $+S_2$ to $+S_3$, which corresponds to a $+45°$ linearly polarized light to a right-handed circularly-polarized light. A little deviation from the straight trajectory will be due to the phase stability in DCSP rather than inherent dynamic response of SLM.

We also investigated hysteresis property of dynamic response in SLM by comparing temporal response of Δ and ψ between rising edge and falling edge of a step-function-like polarization change. Here, the principle polarization axis of the SLM was slightly tilted from x-polarization component to change both Δ and ψ by the change of SLM grayscale value. We measured Δ and ψ at a sampling interval of 9.52 ms. Figures 5(a) and 5(b) respectively show temporally magnified plots of Δ and ψ when the SLM grayscale level in the solid image was increased from 0 to 30. Δ increases while ψ decreases. We determined the time constant of these slopes to be 84 ms for Δ and 82 ms for ψ by the curve fitting analysis with an exponential decay function. It is reasonable that Δ and ψ shows dynamic behavior similar to each other because SLM controls Δ and ψ by changing the alignment direction of liquid crystal molecules with the external electric field. Figures 5(c) and 5(d) respectively show temporally magnified plots of Δ and ψ when the SLM grayscale level was decreased from 30 to 0. We confirmed the temporal behavior of Δ and ψ opposite to that in Figs. 5(a) and 5(b). The reason for the opposite trend is due to the tilt angle of the principle polarization axis of the SLM. If the principle polarization axis of the SLM is set to be the opposite direction, the trend of Δ and ψ is coincide with each other. Time constants of these slopes were determined to be 32 ms for Δ and 37 ms for ψ, which are in significant agreement with each other again. More importantly, time constants in Figs. 5(a) and 5(b) was significantly different from those in Figs. 5(c) and 5(d). We clearly confirmed the hysteresis property of dynamic response in SLM.

4. DISCUSSION

We discuss the reason for hysteresis property of dynamic response in SLM. Under no external electric field, cylindrical molecules of nematic liquid crystal are oriented in parallel to a surface of SLM and perpendicularly to an incident direction of light beam. When the external electric filed is applied in parallel to the incident direction of light beam, a long axis of liquid-crystalline molecules is aligned along the axis of the external electric filed depending on its field strength. SLM controls the polarization of incident light via the birefringence of liquid-crystalline molecules caused by their aligned direction depending on the applied external electric field. When the external electric field is increased as a step function, liquid-crystalline molecules are transiently affected by both the forced driving force and the inertial restoring force, which are opposite to each other. On the other hand, when the external electric field is decreased as a step function, only the inertial restoring force affects liquid-crystalline molecules. Such difference of contributed force between the step-like-increased and step-like-decreased external electric field leads to hysteresis property of dynamic response in SLM.

We next discuss a possibility to further increase the data acquisition rate Δf_{rep} and broaden the spectral bandwidth Δv in DCSP. Δv is related with Δf_{rep} and frep1 as follows

$$\Delta v = \frac{f_{rep1}(f_{rep1} + \Delta f_{rep})}{2\Delta f_{rep}} \approx \frac{f_{rep1}{}^2}{2\Delta f_{rep}}. \tag{9}$$

For example, in the present setup (frep1 ≈ 100 MHz, Δfrep ≈ 1 kHz), Δv is estimated to be 5 THz, corresponding to a wavelength range of 1550 ± 20 nm. In other words, even though OFC has sufficiently broad bandwidth of optical spectrum, the effective spectral bandwidth is limited to avoid the aliasing effect as indicated by Eq. (9). This wavelength range may be still insufficient for some applications of DCSP. From Eq. (9), increase of Δf_{rep} leads to reduction of Δv whereas Δv is quadratic of f_{rep1}. Therefore, increase of Δf_{rep} and Δv can be achieved by increasing both Δf_{rep} and f_{rep1}. Fortunately, increase of f_{rep1}, corresponding to decrease of spectral resolution, is acceptable to DCSP because most of samples in DCSP does not indicate so sharp spectral features. Furthermore, increase of frep1 without the change of total power and spectral bandwidth leads to increase of mode power in OFC and hence increase of signal-to-noise ratio in DCSP, enabling no signal-accumulation measurement at an acquisition rate of Δf_{rep}. There are a few candidates for higher-f_{rep} or GHz-spacing OFCs: electro-optic OFC [28, 29], quantum-cascade-laser OFC [30, 31], and microcomb [32, 33]. Such OFCs were effectively applied for higher-Δf_{rep} DCS [29, 31, 33] together with nonlinear spectral broadening.

For example, in the case of DCSP with f_{rep1} of 10 GHz and Δf_{rep} of 500 kHz, Δv is increased up to 100 THz, corresponding to a wavelength range of 1550 ± 400 nm. In this way, there is still room for enhancement of the data acquisition rate and the spectral bandwidth by selection of OFCs.

5. DISCUSSION

We demonstrated the dynamic characterization of polarization property in LCOS-SLM by DCSP. The proposed DCSP system has a potential to boost the scan rate of Δ and ψ spectra measurement up to 1050 Hz due to the direct polarization determination without the need for polarization modulation benefitting from DCS-based polarimetry. Effectiveness of DCSP was highlighted by visualizing the hysteresis property of dynamic response in SLM at a sampling rate of 105 Hz, indicating the dynamic interaction between the forced driving force and the inertial restoring force in liquid-crystalline molecules of SLM. Although the achieved data acquisition rate and the spectral bandwidth in this article may be still insufficient for some applications of dynamic SP, DCSP has a sufficient room to further boost the data acquisition rate and broaden the spectral bandwidth by use of GHz-spacing OFCs. DCSP will be a powerful tool for dynamic characterization of various samples.

REFERENCES

[1] P. Löper, M. Stuckelberger, B. Niesen, J. Werner, M. Filipič, S. J. Moon, J. H. Yum, M. Topič, S. D. Wolf, and C. Ballif, "Complex refractive index spectra of CH3NH3PbI3 perovskite thin films determined by spectroscopic ellipsometry and spectrophotometry," J. Phys. Chem. Lett. 6(1), 66–71 (2015).

[2] C. Yim, M. O'Brien, N. McEvoy, S. Winters, I. Mirza, J. G. Lunney, and G. S. Duesberg, "Investigation of the optical properties of MoS2 thin films using spectroscopic ellipsometry," Appl. Phys. Lett. 104(10), 103114 (2014).

[3] F. L. McCrackin, E. Passaglia, R. R. Stromberg, and H. L. Steinberg, "Measurement of the thickness and refractive index of very thin films and the optical properties of surfaces by ellipsometry," J. Res. Natl. Bur. Stand., Sect. A 67A(4), 363–377 (1963).

[4] S. G. Lim, S. Kriventsov, and T. N. Jackson, "Dielectric functions and optical bandgaps of high-K dielectrics for metal-oxide-semiconductor field-effect transistors by far ultraviolet spectroscopic ellipsometry," J. Appl. Phys. 91(7), 4500–4505 (2002).

[5] H. L. Liu, C. C. Shen, S. H. Su, C. L. Hsu, M. Y. Li, and L. J. Li, "Optical properties of monolayer transition metal dichalcogenides probed by spectroscopic ellipsometry," Appl. Phys. Lett. 105(20), 201905 (2014).

[6] H. Arwin, "Is ellipsometry suitable for sensor applications?" Sens. Actuators, A 92(1-3), 43–51 (2001).

[7] K. Spaeth, A. Brecht, and G. Gauglitz, "Studies on the biotin-avidin multilayer adsorption by spectroscopic ellipsometry," J. Colloid Interface Sci. 196(2), 128–135 (1997).

[8] Z. H. Wang and G. Jin, "A label-free multisensing immunosensor based on imaging ellipsometry," Anal. Chem. 75(22), 6119–6123 (2003).

[9] D. E. Aspnes, "Fourier transform detection system for rotating-analyzer ellipsometers," Opt. Commun. 8(3), 222–225(1973).

[10] P. S. Hauge and F. H. Dill, "A rotating-compensator Fourier ellipsometer," Opt. Commun. 14(4), 431–437 (1975).

[11] C. Y. Han and Y. F. Chao, "Photoelastic modulated imaging ellipsometry by stroboscopic illumination technique," Rev. Sci. Instrum. 77(2), 023107 (2006).

[12] T. Udem, J. Reichert, R. Holzwarth, and T. W. Hänsch, "Accurate measurement of large optical frequency differences with a mode-locked laser," Opt. Lett. 24(13), 881–883 (1999).

[13] M. Niering, R. Holzwarth, J. Reichert, P. Pokasov, T. Udem, M. Weitz, T. W. Hänsch, P. Lemonde, G. Santarelli, M. Abgrall, P. Laurent, C. Salomon, and A. Clairon, "Measurement of the hydrogen 1S-2S transition frequency by phase coherent comparison with a microwave cesium fountain clock," Phys. Rev. Lett. 84(24), 5496–5499 (2000).

[14] T. Udem, R. Holzwarth, and T. W. Hänsch, "Optical frequency metrology," Nature 416(6877), 233–237 (2002).

[15] S. Schiller, "Spectrometry with frequency combs," Opt. Lett. 27(9), 766–768 (2002).

[16] F. Keilmann, C. Gohle, and R. Holzwarth, "Time-domain mid-infrared frequency-comb spectrometer," Opt. Lett. 29(13), 1542–1544 (2004).

[17] T. Yasui, Y. Kabetani, E. Saneyoshi, S. Yokoyama, and T. Araki, "Terahertz frequency comb by multifrequency-heterodyning photoconductive detection for high-accuracy, high-resolution terahertz spectroscopy," Appl. Phys. Lett. 88(24), 241104 (2006).

[18] Coddington, N. Newbury, and W. Swann, "Dual-comb spectroscopy," Optica 3(4), 414–426 (2016).

[19] S. Okubo, K. Iwakuni, H. Inaba, K. Hosaka, A. Onae, H. Sasada, and F. L. Hong, "Ultra-broadband dual-comb spectroscopy across 1.0–1.9μm," Appl. Phys. Express 8(8), 082402 (2015).

[20] H. Koresawa, K. Shibuya, T. Minamikawa, A. Asahara, R. Oe, T. Mizuno, M. Yamagiwa, Y. Mizutani, T. Iwata, H. Yamamoto, K. Minoshima, and T. Yasui, "Lock-in-detection dual-comb spectroscopy," OSA Continuum 2(6), 1998–2007 (2019).

[21] Y. Shimizu, S. Okubo, A. Onae, K. M. T. Yamada, and H. Inaba, "Molecular gas thermometry on acetylene using dual-comb spectroscopy: analysis of rotational energy distribution," Appl. Phys. B: Lasers Opt. 124(4), 71 (2018).

[22] Asahara, A. Nishiyama, S. Yoshida, K. Kondo, Y. Nakajima, and K. Minoshima, "Dual-comb spectroscopy for rapid characterization of complex optical properties of solids," Opt. Lett. 41(21), 4971–4974 (2016).

[23] K. Shibuya, T. Minamikawa, Y. Mizutani, H. Yamamoto, K. Minoshima, T. Yasui, and T. Iwata, "Scan-less hyperspectral dual-comb single-pixel-imaging in both amplitude and phase," Opt. Express 25(18), 21947–21957(2017).

[24] T. Ideguchi, S. Holzner, B. Bernhardt, G. Guelachvili, N. Picqué, and T. W. Hänsch, "Coherent Raman spectro-imaging with laser frequency combs," Nature 502(7471), 355–358 (2013).

[25] K. A. Sumihara, S. Okubo, M. Okano, H. Inaba, and S. Watanabe, "Polarization-sensitive dual-comb spectroscopy," J. Opt. Soc. Am. B 34(1), 154–159 (2017).

[26] K. A. Sumihara, S. Okubo, K. Oguchi, M. Okano, H. Inaba, and S. Watanabe, "Polarization-sensitive dual-comb spectroscopy with an electro-optic modulator for determination of anisotropic optical responses of materials," Opt. Express 27(24), 35141–35165 (2019).

[27] T. Minamikawa, Y. Hsieh, K. Shibuya, E. Hase, Y. Kaneoka, S. Okubo, H. Inaba, Y. Mizutani, H. Yamamoto, T. Iwata, and T. Yasui, "Dual-comb spectroscopic ellipsometry," Nat. Commun. 8(1), 610 (2017).

[28] T. Kawanishi, T. Sakamoto, S. Shinada, and M. Izutsu, "Optical frequency comb generator using optical fiber loops with single-sideband modulation," IEICE Electron. Express 1(8), 217–221 (2004).

[29] M. M. Pedro, B. Jerez, and P. Acedo, "Dual electro-optic optical frequency combs for multiheterodyne molecular dispersion spectroscopy," Opt. Express 23(16), 21149–21158 (2015).

[30] Hugi, G. Villares, S. Blaser, H. C. Liu, and J. Faist, "Mid-infrared frequency comb based on a quantum cascade laser," Nature 492(7428), 229–233 (2012).

[31] G. Villares, A. Hugi, S. Blaser, and J. Faist, "Dual-comb spectroscopy based on quantum-cascade-laser frequency combs," Nat. Commun. 5(1), 5192 (2014).

[32] P. Del'Haye, A. Schliesser, O. Arcizet, T. Wilken, R. Holzwarth, and T. J. Kippenberg, "Optical frequency comb generation from a monolithic microresonator," Nature 450(7173), 1214–1217 (2007).

[33] M. G. Suh, Q. F. Yang, K. Y. Yang, X. Yi, and K. J. Vahala, "Microresonator soliton dual-comb spectroscopy," Science 354(6312), 600–603 (2016).